Application of the Generalized Spectral-Domain Technique to the Analysis of Rectangular Waveguides with Rectangular and Circular Metal Inserts

Abbas S. Omar, *Senior Member, IEEE* and Klaus F. Schünemann, *Senior Member, IEEE*

Abstract—**The generalized spectral-domain (GSD) technique, which was developed and tested for some special cases in [1], is applied to the analysis of rectangular waveguides with rectangular and circular metal inserts. These include conventional ridge waveguides, circular-ridge waveguides, and rectangular coaxial lines with either rectangular or circular inner conductors. The numerical results show that the edge behavior of the electromagnetic field described in [2] is incomplete. A constant term must be added to the expansion of the magnetic field component which is parallel to the edge. Excellent agreement with other publications is achieved, with a drastic reduction of CPU time for the conventional ridge waveguide. The accuracy of the results is demonstrated by two- and three-dimensional plots of the field distributions.**

I. Introduction

GALERKIN's method in the spectral domain, which is known in the literature simply as the spectral-domain (SD) technique, has been developed and applied to the analysis of a variety of planar structures (see, e.g., [3]–[7]). It has proved to be a very efficient method with respect to accuracy, CPU time, and storage requirements. On the other hand, the method is restricted to the analysis of structures with infinitely thin metal sheets.

In the general analysis of waveguides with metal inserts, which was recently presented in [1], two formulations have been developed: the matrix formulation and the moment method formulation. The latter is a generalization of the SD technique which can analyze waveguides with electrically thick metal inserts as well. It will be called the generalized spectral-domain (GSD) technique. It has been shown in [1] that applying the GSD technique to planar structures leads to the same equations as the conventional SD technique. In this paper, the GSD technique is applied to rectangular waveguides with rectangular or circular metal inserts. These include conventional ridge waveguides, ridge waveguides with half circular ridges, and rectangular coaxial waveguides with either rectangular or circular inner conductors.

According to [1], the axial magnetic field or the normal electric field at the surface of the metal insert is expanded with respect to suitable basis functions which satisfy the edge conditions, if any. The vanishing of the tangential electric field or the normal magnetic field at the metal surface is then tested by the same basis functions (Galerkin's procedure). If the basis functions for the axial magnetic field are chosen to satisfy the edge conditions given in [2], the resulting field would not identically vanish inside the metal insert. Such basis functions must become zero as the edge is approached [2]. The right field can be obtained if an additional basis function is used, which becomes a constant as the edge is approached. This is an indication that the edge conditions described in [2] are not complete.

II. Basic Formulation

Consider the waveguide with metal insert shown in Fig. 1. The direction of propagation, in which the structure is uniform, is taken along the z axis with a corresponding propagation constant β. As has been shown in [1], TE modes are expressed as

$$h_z = \sum_n \frac{a_n^{(h)}}{\sqrt{P_{nh}}} k_{nh}^2 h_{zn}$$

$$\boldsymbol{h} = -j\beta \left[\sum_n \frac{a_n^{(h)}}{\sqrt{P_{nh}}} \nabla_t h_{zn} + \sum_n \frac{b_n^{(h)}}{\sqrt{P_{ne}}} (\nabla_t e_{zn} \times \hat{\boldsymbol{k}}) \right]$$

$$\boldsymbol{e} = \frac{\omega \mu_0}{\beta} (\boldsymbol{h} \times \hat{\boldsymbol{k}}) \tag{1}$$

where h_z, $\boldsymbol{h}$, and $\boldsymbol{e}$ are the axial magnetic, transverse magnetic, and transverse electric field, respectively, with the z dependence $e^{-j\beta z}$ being suppressed, h_{zn} (e_{zn}) is the axial magnetic (electric) field of the nth TE (TM) mode in the hollow waveguide (i.e., with the metal insert S_0 removed), and k_{nh} (k_{ne}) is the corresponding cutoff wave-

Manuscript received September 26, 1990; revised January 17, 1991.

The authors are with the Arbeitsbereich Hochfrequenztechnik, Technische Universität Hamburg–Harburg, Postfach 90 10 52, D-2100 Hamburg 90, Germany.

IEEE Log Number 9144288.

0018-9480/91/0600-0944$01.00 ©1991 IEEE

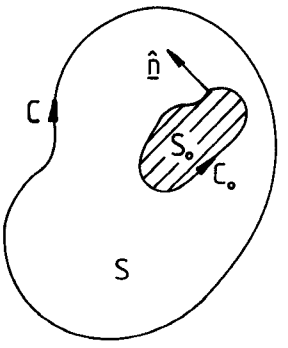

Fig. 1. Cross section of a waveguide with a metal insert.

number. P_{nh} (P_{ne}) is the integral of h_{zn}^2 (e_{zn}^2) over the hollow waveguide cross section S; ∇_t and $\hat{k}$ are the transverse component of the del operator and the unit vector in the axial direction, respectively; and $a_n^{(h)}$ and $b_n^{(h)}$ are expansion coefficients to be determined.

According to the moment method formulation [1], the axial magnetic field, h_{zn} at the contour C_0 is expanded in terms of suitable basis functions η_i as

$$h_z|_{c_0} = \sum_i I_i \eta_i. \tag{2}$$

The expansion coefficients $a_n^{(h)}$ and $b_n^{(h)}$ are given in terms of I_t according to

$$\boldsymbol{a}^{(h)} = [\Lambda^h]^{-1/2}\left([\Lambda^h] - k_c^2[I]\right)^{-1}[C^{hh}]\boldsymbol{I}$$

$$\boldsymbol{b}^{(h)} = \frac{1}{k_c^2}[\Lambda^e]^{-1/2}[C^{he}]\boldsymbol{I}. \tag{3}$$

Here $\boldsymbol{a}^{(h)}$, $\boldsymbol{b}^{(h)}$, and $\boldsymbol{I}$ are column vectors with elements $a_n^{(h)}$, $b_n^{(h)}$, and I_i, respectively; $[\Lambda^h]$ ($[\Lambda^e]$) is a diagonal matrix with elements k_{nh}^2 (k_{ne}^2), $[I]$ is the identity matrix; and k_c is the yet undetermined cutoff wavenumber ($k_c^2 = k_0^2 - \beta^2$). The elements of $[C^{hh}]$ and $[C^{he}]$ are given by

$$C_{ni}^{hh} = \frac{1}{k_{nh}\sqrt{P_{nh}}} \oint_{C_0} \eta_i (\hat{n}\cdot\nabla_t h_{zn})\, dl$$

$$C_{ni}^{he} = \frac{1}{k_{ne}\sqrt{P_{ne}}} \oint_{C_0} \eta_i \left((\hat{n}\times\hat{k})\cdot\nabla_t e_{zn}\right) dl. \tag{4}$$

k_c^2 and the corresponding $\boldsymbol{I}$ are determined by solving the characteristic equation

$$\left\{k_c^2[C^{hh}]^t\left(k_c^2[I] - [\Lambda^h]\right)^{-1}[C^{hh}] + [C^{he}]^t[C^{he}]\right\}\boldsymbol{I} = [Z]\,\boldsymbol{I} = 0 \tag{5}$$

where the superscript t denotes the transpose of the matrix. TM modes, on the other hand, are expressed as

$$e_z = \frac{-k_c^2}{j\beta}\sum_n \frac{a_n^{(e)}}{\sqrt{P_{ne}}} e_{zn}$$

$$\boldsymbol{e} = \sum_n \frac{a_n^{(e)}}{\sqrt{P_{ne}}}\nabla_t e_{zn}$$

$$\boldsymbol{h} = \frac{\omega\epsilon_0}{\beta}(\hat{k}\times\boldsymbol{e}) \tag{6}$$

where e_z is the axial electric field and $a_n^{(e)}$ are expansion coefficients to be determined. Expanding the normal electric field $(\hat{n}\cdot\boldsymbol{e})$ at the contour C_0 in terms of suitable basis function ξ_t as

$$(\hat{n}\cdot\boldsymbol{e})|_{C_0} = \sum_i V_t \xi_i \tag{7}$$

the expansion coefficients $a_n^{(e)}$ are given in terms of V_i according to

$$\boldsymbol{a}^{(e)} = \left(k_c^2[I] - [\Lambda^e]\right)^{-1}[C^{ee}]V \tag{8}$$

where $\boldsymbol{a}^{(e)}$ and V are column vectors with elements $a_n^{(e)}$ and V_t, respectively. The elements of $[C^{ee}]$ are given by

$$C_{ni}^{ee} = \frac{1}{\sqrt{P_{ne}}} \oint_{C_0} \xi_t e_{zn}\, dl. \tag{9}$$

k_c^2 and the corresponding V are determined by solving the characteristic equation

$$[C^{ee}]^t\left(k_c^2[I] - [\Lambda^e]\right)^{-1}[C^{ee}]V = [Y]V = 0. \tag{10}$$

III. Rectangular Inserts

Fig. 2(a) shows the cross section of a conventional ridge waveguide, while Fig. 2(b) shows that of a rectangular coaxial line. The rectangular coaxial line has recently been proposed [8] for applications in communication satellites. If we utilize symmetry, only one quarter of either structure needs to be analyzed, e.g. That shown in Fig. 2(c).

If h_z and $(\hat{n}\cdot\boldsymbol{e})$ in (2) and (7), respectively, are rewritten as

$$h_z|_{C_0} = \begin{cases} h_z|_{y=y_0} = \sum_i I_i^{(1)}\eta_i^{(1)}(x), & 0 \le x \le x_0 \\ h_z|_{x=x_0} = \sum_i I_i^{(2)}\eta_i^{(2)}(y), & y_0 \le y \le b \end{cases} \tag{11}$$

$$(\hat{n}\cdot\boldsymbol{e})|_{C_0} = \begin{cases} -e_y|_{y=y_0} = \sum_t V_t^{(1)}\xi_i^{(1)}(x), & 0 \le x \le x_0 \\ +e_x|_{x=x_0} = \sum_i V_t^{(2)}\xi_t^{(2)}(y), & y_0 \le y \le b \end{cases} \tag{12}$$

the characteristic equations in (5) and (10), respectively, can be written as

$$\begin{bmatrix} [Z^{(11)}] & [Z^{(12)}] \\ [Z^{(21)}] & [Z^{(22)}] \end{bmatrix}\begin{bmatrix} \boldsymbol{I}^{(1)} \\ \boldsymbol{I}^{(2)} \end{bmatrix} = 0 \tag{13}$$

$$\begin{bmatrix} [Y^{(11)}] & [Y^{(12)}] \\ [Y^{(21)}] & [Y^{(22)}] \end{bmatrix}\begin{bmatrix} V^{(1)} \\ V^{(2)} \end{bmatrix} = 0 \tag{14}$$

where $\boldsymbol{I}^{(1)}$, $\boldsymbol{I}^{(2)}$, $V^{(1)}$, and $V^{(2)}$ are column vectors with elements $I_t^{(1)}$, $I_t^{(2)}$, $V_t^{(1)}$, and $V_t^{(2)}$, respectively.

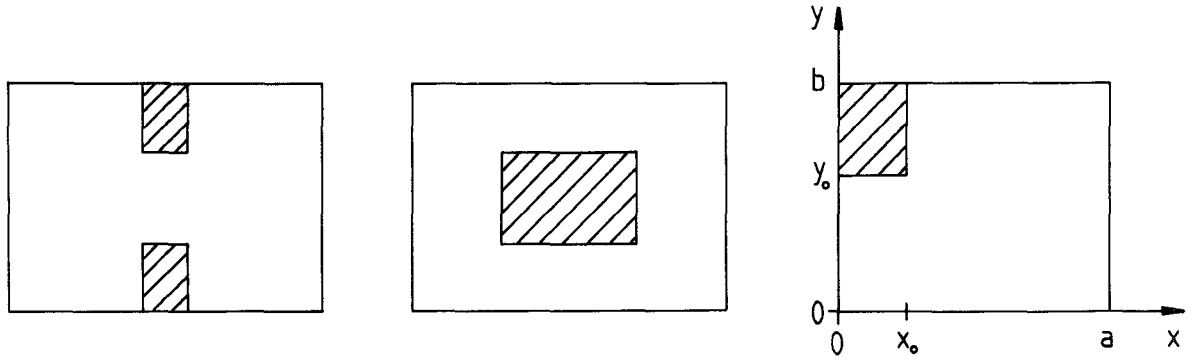

Fig. 2. (a) Cross section of a conventional ridge waveguide. (b) Cross section of a rectangular coaxial line. (c) A quarter of either structure.

TE Modes

Only one type of symmetry will be considered, namely that with a magnetic wall at side $x = 0$ and electric walls at the other three sides. Modes with this type of symmetry include the dominant mode of the symmetrical ridge waveguide. Other types of symmetry can similarly be analyzed. The basis functions $\eta_i^{(1)}(x)$ and $\eta_i^{(2)}(y)$, which satisfy the 90° edge conditions at (x_0, y_0), must behave like $|x - x_0|^{2/3}$ and $|y - y_0|^{2/3}$ as $x \to x_0$ and $y \to y_0$, respectively, [2]. They are given by

$$\eta_i^{(1)}(x) = \left[1 - \left(\frac{x}{x_0}\right)^2\right]^{-1/3} \sin\frac{i\pi x}{x_0}$$

$$\eta_i^{(2)}(y) = \left[1 - \left(\frac{b-y}{b-y_0}\right)^2\right]^{-1/3} \cos\frac{(i-1/2)\pi(b-y)}{(b-y_0)}, \qquad i = 1, 2, \cdots. \quad (15)$$

Following the procedure described in [1] for TM modes, the elements of the $[Z]$ matrix in (13) are given by

$$Z_{ij}^{(11)} = -\frac{\pi a}{2b}\sum_{n=1}^{\infty} \bar{\alpha}_n \frac{\sin\bar{\alpha}_n(\pi-\psi_0)\sin\bar{\alpha}_n\psi_0}{\sin\bar{\alpha}_n\pi}\tilde{\eta}_{in}^{(1)}\tilde{\eta}_{jn}^{(1)}$$

$$Z_{ij}^{(12)} = \frac{\pi b}{2a}\sum_{n=1}^{\infty}(n-1/2) \cdot \frac{\cos(n-1/2)\varphi_0 \sin\bar{\alpha}_n\psi_0}{\sin\bar{\alpha}_n\pi}\tilde{\eta}_{in}^{(1)}\bar{\tilde{\eta}}_{jn}^{(2)} = Z_{ji}^{(21)}$$

$$Z_{ij}^{(22)} = -\frac{\pi b}{2a}\sum_{m=0}^{\infty}(1+\delta_{m0})\bar{\gamma}_m \cdot \frac{\sin\bar{\gamma}_m(\pi-\varphi_0)\cos\bar{\gamma}_m\varphi_0}{\cos\bar{\gamma}_m\pi}\tilde{\eta}_{im}^{(2)}\tilde{\eta}_{jm}^{(2)} \quad (16)$$

where

$$\bar{\alpha}_n = \frac{b}{\pi}\sqrt{k_c^2 - \left(\frac{(n-1/2)\pi}{a}\right)^2}$$

$$\bar{\gamma}_m = \frac{a}{\pi}\sqrt{k_c^2 - \left(\frac{m\pi}{b}\right)^2}$$

$$\varphi_0 = \frac{\pi x_0}{a} \qquad \psi_0 = \frac{\pi y_0}{b}$$

$$\tilde{\eta}_{in}^{(1)} = K\varphi_0\left[\frac{J_\nu(i\pi-(n-1/2)\varphi_0)}{(i\pi-(n-1/2)\varphi_0)^\nu} - \frac{J_\nu(i\pi+(n-1/2)\varphi_0)}{(i\pi+(n-1/2)\varphi_0)^\nu}\right]$$

$$\tilde{\eta}_{im}^{(2)} = K(-1)^m\frac{(\pi-\psi_0)}{(1+\delta_{m0})}\left[\frac{J_\nu((i-1/2)\pi-m(\pi-\psi_0))}{((i-1/2)\pi-m(\pi-\psi_0))^\nu} + \frac{J_\nu((i-1/2)\pi+m(\pi-\psi_0))}{((i-1/2)\pi+m(\pi-\psi_0))^\nu}\right]$$

$$\bar{\tilde{\eta}}_{in}^{(2)} = K(\pi-\psi_0)\left[\frac{J_\nu((i-1/2)\pi-\bar{\alpha}_n(\pi-\psi_0))}{((i-1/2)\pi-\bar{\alpha}_n(\pi-\psi_0))^\nu} + \frac{J_\nu((i-1/2)\pi+\bar{\alpha}_n(\pi-\psi_0))}{((i-1/2)\pi+\bar{\alpha}_n(\pi-\psi_0))^\nu}\right] \quad (17)$$

where $K = 2^{-5/6}\pi^{-1/2}\Gamma(2/3) = 0.428769$, $J_\nu(x) =$ Bessel function of the first kind, $\nu = 1/6$, and $\delta_{m0} =$ Kronecker delta.

If the convergence of the series in (16) is investigated, it can easily be shown that the sum terms in $Z_{ij}^{(11)}$ and $Z_{ij}^{(12)}$ behave like $n^{-7/3}$ as $n \to \infty$ and that the sum term in $Z_{ij}^{(22)}$ behaves like $m^{-7/3}$ as $m \to \infty$ (see, e.g., [9] for the asymptotic value of the Bessel functions).

The axial magnetic field as given by (11) and (15) vanishes at the edge (x_0, y_0). The numerical results based on this assumption, however, turned out to be incorrect. Fig. 3 shows a three-dimensional plot of the axial magnetic field, h_z, corresponding to the dominant mode in a ridge waveguide as a function of the transverse coordinates. Although the field possesses a step discontinuity at the ridge surfaces, it does not identically vanish over the

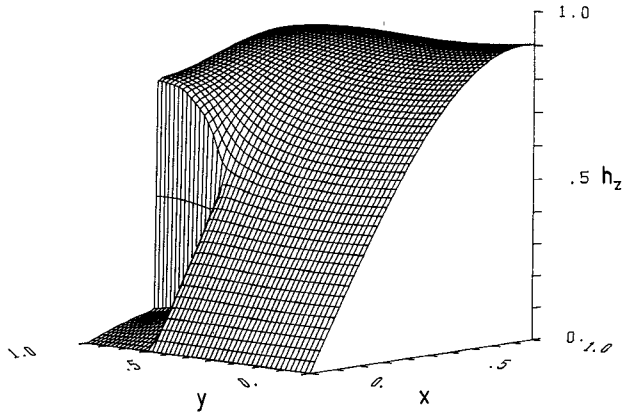

Fig. 3. A three-dimensional plot of the axial magnetic field, h_z, corresponding to the dominant mode in a ridge waveguide (the basis functions in (18) are not considered). Parameters: $(a/b)=1.0$, $(x_0/a)=0.3$, $(y_0/a)=0.7$.

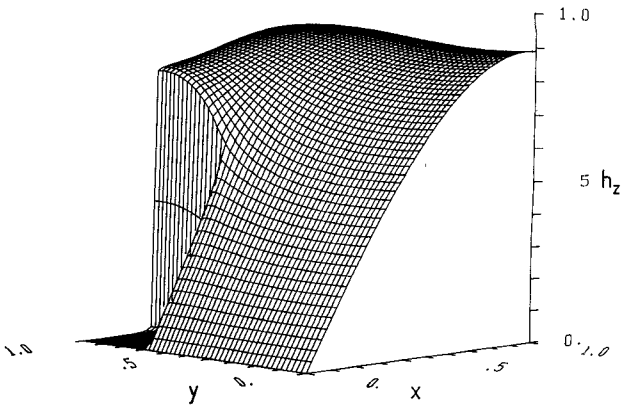

Fig. 4. The same plot as in Fig. 3, with the basis functions in (18) considered.

ridge. This effect is found to be independent of the number of basis functions in (15), which indicates that these functions are not a complete set.

A detailed investigation of the edge conditions derived in [2] has shown that the edge behavior of the magnetic field component which is parallel to the edge has been assumed to be identical to that of the corresponding electric field component. This assumption is, however, incorrect because of the different boundary conditions which must be satisfied by these two components. The derivation of the edge conditions given in [10] shows that although the electric field component which is parallel to the edge must vanish at the edge, the corresponding magnetic field component can approach a constant value there. The higher spatial derivatives of the two components are similar and obey the analysis of [2]. This explains the incompleteness of the basis functions given in (15), which vanish at the edge. Additional basis functions, which approach a constant value at the edge, are hence necessary.

The analysis presented above remains valid if the following basis functions are added to those given in (15):

$$\eta_0^{(1)}(x)=\sin\frac{\pi x}{2x_0}$$

$$\eta_0^{(2)}(y)=1. \tag{18}$$

The corresponding Fourier transforms cannot be incorporated in (17) with $i=0$ because (17) is valid only for the basis functions given in (15). Instead, they are given by

$$\tilde{\eta}_{0n}^{(1)}=\frac{2\varphi_0^2}{\pi}\frac{(n-1/2)\cos(n-1/2)\varphi_0}{\left[(\pi/2)^2-(n-1/2)^2\varphi_0^2\right]}$$

$$\tilde{\eta}_{0m}^{(2)}=\frac{2}{\pi(1+\delta_{m0})}(-1)^m\frac{\sin m(\pi-\psi_0)}{m}$$

$$\bar{\tilde{\eta}}_{0n}^{(2)}=\frac{2}{\pi\bar{\alpha}_n}\sin\bar{\alpha}_n(\pi-\psi_0). \tag{19}$$

Investigating the convergence of series in (16) for $(i\neq 0, j=0)$ shows that the sum terms in $Z_{i0}^{(11)}$, $Z_{i0}^{(12)}$, and $Z_{i0}^{(22)}$ behave like $n^{-5/3}$, $n^{-5/3}$, and $m^{-5/3}$ as $n\to\infty$ and $m\to\infty$, respectively, which means that the series are still convergent. On the other hand, $Z_{00}^{(11)}$, $Z_{00}^{(12)}$, and $Z_{00}^{(22)}$ do not converge at all because their sum terms behave like n^{-1}, n^{-1}, and m^{-1} as $n\to\infty$ and $m\to\infty$, respectively. This numerical problem arises because the two basis functions $\eta_0^{(1)}(x)$ and $\eta_0^{(2)}(y)$ are weighted in (11) by two different expansion coefficients $I_0^{(1)}$ and $I_0^{(2)}$, respectively. On the other hand, h_z must approach one and the same constant as $x\to x_0$ or as $y\to y_0$, which means that $I_0^{(1)}=I_0^{(2)}$.

If the two unknowns $I_0^{(1)}$ and $I_0^{(2)}$ are set equal in the matrix equation (13), the corresponding columns appear to be added together ($Z_{i0}^{(11)}$ and $Z_{i0}^{(21)}$ are added to $Z_{i0}^{(12)}$ and $Z_{i0}^{(22)}$, respectively), thus forming a single column. In order to maintain the symmetry of the $[Z]$ matrix, the row with elements $Z_{0j}^{(11)}$ and $Z_{0j}^{(12)}$ will be added to that with elements $Z_{0j}^{(21)}$ and $Z_{0j}^{(22)}$, respectively, thus forming a single row. This leads to

$$Z_{i0}^{(11)}+Z_{i0}^{(12)}=-\frac{\pi b}{2a}\left[\left(\frac{k_c a}{\pi}\right)^2-\left(\frac{\pi}{2\varphi_0}\right)^2\right]\cdot\sum_{n=1}^{\infty}\frac{\sin\bar{\alpha}_n(\pi-\psi_0)\sin\bar{\alpha}_n\psi_0}{\bar{\alpha}_n\sin\bar{\alpha}_n\pi}\tilde{\eta}_{in}^{(1)}\tilde{\eta}_{0n}^{(1)}$$

$$Z_{i0}^{(21)}+Z_{i0}^{(22)}=-\frac{\pi b}{2a}\varphi_0^2\left[\left(\frac{k_c a}{\pi}\right)^2-\left(\frac{\pi}{2\varphi_0}\right)^2\right]\cdot\sum_{m=0}^{\infty}(1+\delta_{m0})\bar{\gamma}_m\frac{\sin\bar{\gamma}_m(\pi-\varphi_0)\cos\bar{\gamma}_m\varphi_0}{\cos\bar{\gamma}_m\pi}\cdot\frac{\tilde{\eta}_{im}^{(2)}\tilde{\eta}_{0m}^{(2)}}{\left[(\pi/2)^2-\bar{\gamma}_m^2\varphi_0^2\right]}. \tag{20}$$

The sum terms in $(Z_{i0}^{(11)}+Z_{i0}^{(12)})$ and $(Z_{i0}^{(21)}+Z_{i0}^{(22)})$ behave like $n^{-11/3}$ and $m^{-11/3}$ for $i\neq 0$ and like n^{-3} and m^{-3} for $i=0$ as $n\to\infty$ and $m\to\infty$, respectively, which guarantees the convergence of the above series.

It is worth noting that the reported incompleteness of the edge conditions given in [2] has no influence on the analysis of structures with infinitely thin metal inserts, e.g.

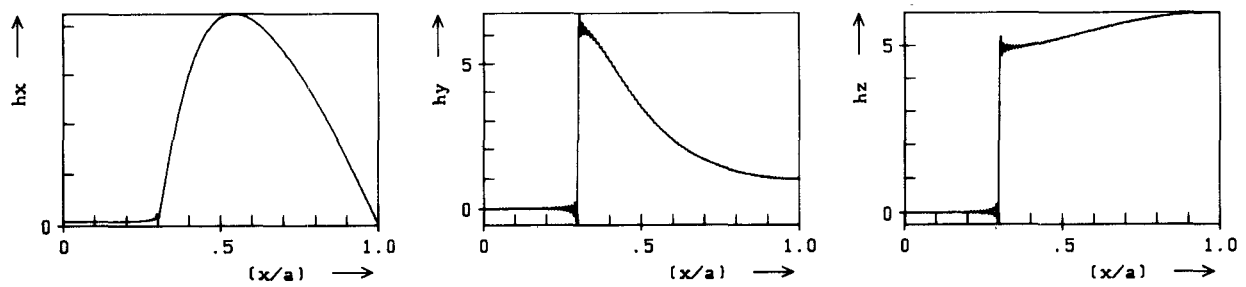

Fig. 5. Plots of the magnetic field components versus x at $(y/a) = 0.85$. Parameters: as in Fig. 3.

TABLE I
CUTOFF WAVENUMBERS (RAD/MM) OF THE FIRST EIGHT MODES IN A SINGLE-RIDGE WAVEGUIDE

Mode	1	2	3	4	5	6	7	8
Present method	0.0928	0.3332	0.3810	0.5262	0.6654	0.6912	0.7456	0.8294
Ref. [11]	0.0930	0.3332	0.3881	0.5265	0.6654	0.6913	0.7456	0.8298

Parameters: $a = b = 9.5$ mm; $x_0 = 0.15$ mm, $y_0 = 1.7$ mm.

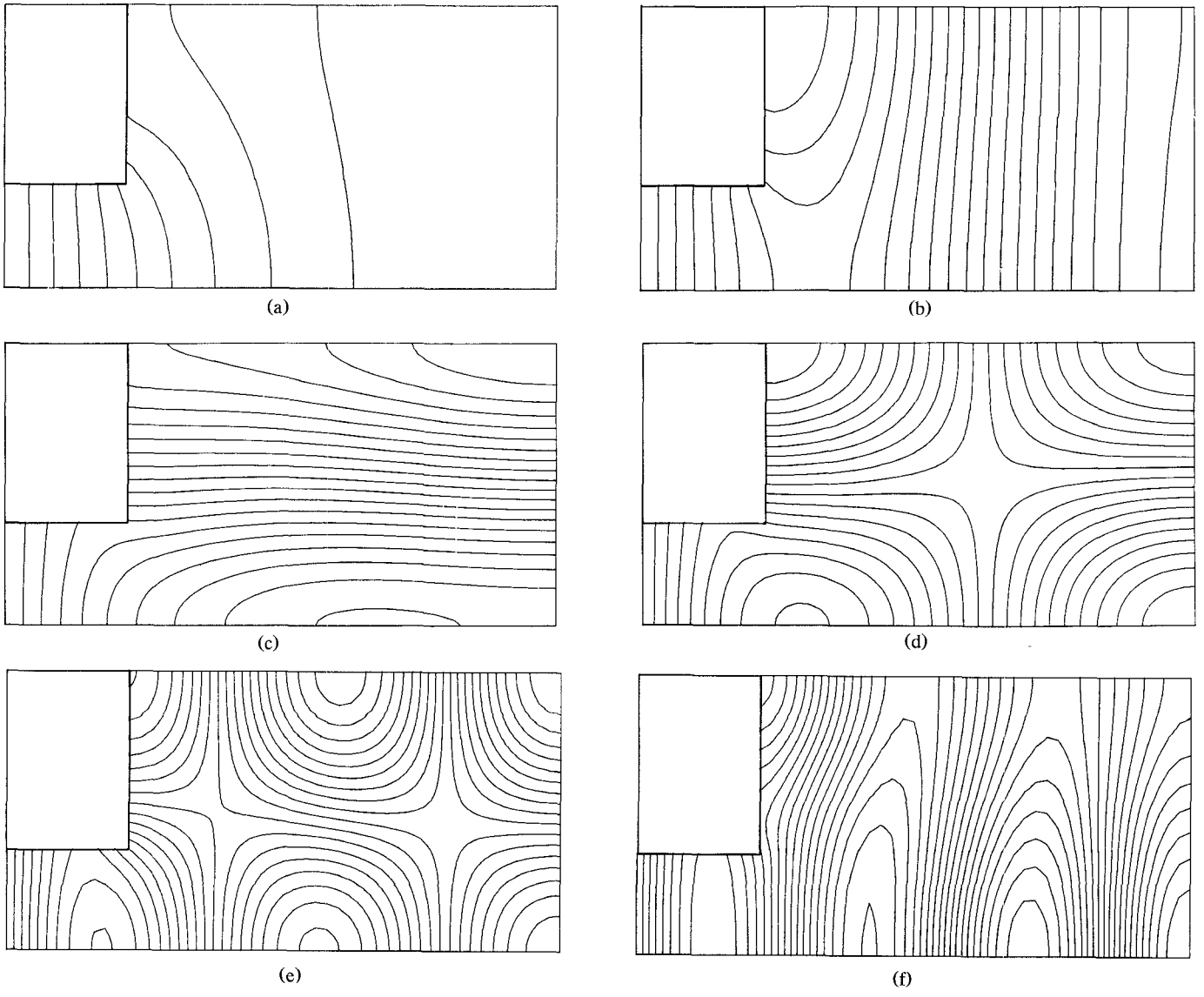

Fig. 6. Electric field lines of the first six modes in a ridge waveguide: (a) first (dominant) mode; (b) second mode; (c) third mode; (d) fourth mode; (e) fifth mode; (f) sixth mode. Parameters: $(b/a) = 0.5$, $(x_0/a) = (y_0/a) = 0.2$.

TABLE II
MODE COUPLING COEFFICIENTS $\tilde{Q}_{ij}$ FOR THE FIRST TEN MODES IN A RIDGE WAVEGUIDE

$ij \rightarrow$ / $\downarrow$	1	2	3	4	5	6	7	8	9	10
1	+1.0000	−0.0005	−0.0002	−0.0003	−0.0002	−0.0005	+0.0001	−0.0003	+0.0002	+0.0000
2		+1.000	−0.0003	−0.0005	−0.0004	−0.0009	+0.0003	−0.0006	+0.0004	+0.0000
3			+1.0000	−0.0005	−0.0004	−0.0002	+0.0000	−0.0004	−0.0010	−0.0003
4				+1.0000	−0.0008	−0.0004	+0.0000	−0.0007	−0.0018	−0.0005
5					+1.0000	−0.0002	+0.0000	−0.0007	−0.0019	−0.0005
6						+1.0000	+0.0001	−0.0003	+0.0005	−0.0001
7							+1.0000	+0.0002	−0.0009	−0.0004
8								+1.0000	−0.0012	−0.0002
9									+1.0000	−0.0025
10										+1.0000

Parameters: as in Fig. 6

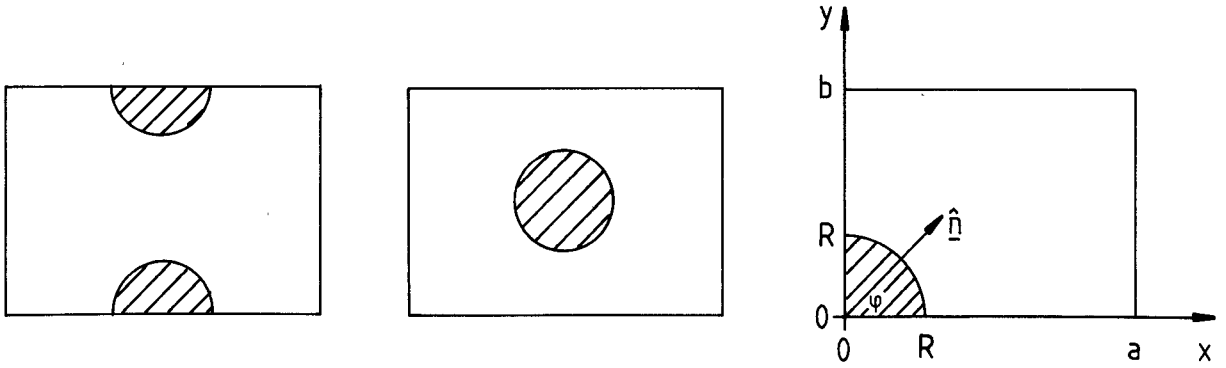

Fig. 7. (a) Cross section of a circular ridge waveguide. (b) Cross section of a shielded metal rod. (c) A quarter of either structure.

planar structures. For these structures the expanded surface current is the difference between the tangential magnetic fields just in front of and just behind the metal insert. The constants approached by the two tangential fields at the edge(s) cancel each other. The surface current component perpendicular to the edge, which is equal to the discontinuity in the magnetic field component parallel to the edge, must then vanish at the edge. This explains why the early work with the SD technique (e.g. in [6] and [7]) failed to detect this incompleteness.

Fig. 4 shows the same plot as Fig. 3 after supplementing the basis functions by (18). The field vanishes now over the ridge and has a step discontinuity at the ridge surfaces. Fig. 5 shows plots for h_x, h_y, and h_z versus x at a $y =$ constant line which goes through the ridge. The tangential components h_y and h_z show step discontinuities at the air–ridge interface, which are accompanied by the so-called Gibbs phenomenon. On the other hand, h_x is continuous there.

A comparison between this method and that presented in [11] is illustrated in Table I, which shows the cutoff wavenumbers of the first eight modes in a single-ridge waveguide. Except for the third mode, for which the error is less than just 2%, the agreement between the two methods is excellent.

The electric field lines of the first six modes in a ridge waveguide with different dimensions are shown in Fig. 6. The field is concentrated below the ridge for the first (dominant) mode only. According to [12], the dominant mode is "hybrid" while the other modes are "trough" because their corresponding fields are distributed everywhere over the cross section.

The accuracy of the field distributions corresponding to the different modes is finally tested by calculating the mode coupling coefficient, which is given by

$$Q_{ij} = \int_{s - s_0} h_z^{(i)} h_z^{(j)}\, dS \tag{21}$$

where $h_z^{(i)}$ is the axial magnetic field corresponding to the ith mode. According to [13, sec. 5.2],

$$\tilde{Q}_{ij} = Q_{ij} / (Q_{ii} Q_{jj})^{1/2} = \delta_{ij}.$$

Table II shows $\tilde{Q}_{ij}$ for the first ten modes. The $\tilde{Q}_{ij}$ resemble their exact values given in [13] to a very great extent.

IV. CIRCULAR INSERTS

Fig. 7(a) shows the cross section of a symmetrical circular ridge waveguide, while Fig. 7(b) shows that of a shielded metal rod. The two guides represent a low-loss alternative to the corresponding guides shown in Fig. 2, where the rectangular metal inserts have been replaced by circular or semicircular ones. The losses for a circular metal inserts are less than those for an equivalent rectangular one because of the absence of sharp edges. As in

the previous case, the structure shown in Fig. 7(c) will be analyzed. Again only one type of symmetry will be considered, namely that with electric walls at all sides.

Because C_0 contains no sharp edges, the basis functions η_i and ξ_i in (2) and (7), respectively, can be chosen as

$$\eta_i(\varphi) = \cos 2i\varphi, \qquad i = 0,1,2,\cdots \tag{22}$$

$$\xi_i(\varphi) = \sin 2i\varphi, \qquad i = 1,2,\cdots. \tag{23}$$

Following a rather lengthy but straightforward procedure, the elements of the $[Z]$ matrix in (5) and of the $[Y]$ matrix in (10), which characterize the TE and TM modes, respectively, are given by

$$Z_{ij} = (-1)^{i+j} \cdot \left[(k_c R)^2 \sum_{n=0}^{\infty} \sum_{m=0}^{\infty} \frac{C_i C_j B_i' B_j'}{(1+\delta_{n0})(1+\delta_{m0})(k_c^2 - k_{nm}^2)} + 4ij \sum_{n=1}^{\infty} \sum_{m=1}^{\infty} \frac{S_i S_j B_i B_j}{k_{nm}^2} \right] \tag{24}$$

$$Y_{ij} = (-1)^{i+j} \sum_{n=1}^{\infty} \sum_{m=1}^{\infty} \frac{S_i S_j B_i B_j}{k_c^2 - k_{nm}^2} \tag{25}$$

where

$$C_i = \cos 2i\alpha_{nm} \qquad S_i = \sin 2i\alpha_{nm}$$

$$B_i = J_{2i}(k_{nm}R) \qquad B_i' = \frac{dJ_{2i}}{dx}\Big|_{x=k_{nm}R}$$

$$k_{nm}^2 = \left(\frac{n\pi}{a}\right)^2 + \left(\frac{m\pi}{b}\right)^2 \qquad \alpha_{nm} = \tan^{-1}\left(\frac{ma}{nb}\right). \tag{26}$$

Fig. 8 shows three-dimensional plots of the axial magnetic field, h_z, and the axial electric field, e_z, corresponding to the first TE mode and the first TM mode, respectively, in a waveguide with the cross section of Fig. 7(c). Both fields vanish over the metal insert. As in Fig. 4, h_z has a step discontinuity at the surface of the insert, which is accompanied by Gibbs's phenomenon. On the other hand, e_z is continuous everywhere.

Table III and Table IV compare the cutoff wavenumbers of the first five TE modes and the first five TM modes, respectively, in a circular ridge waveguide with those in a conventional ridge waveguide with the same ridge cross-sectional area. The cutoff wavenumbers (and hence the propagation constants and the wave impedances) of the corresponding modes differ very little, which indicates that the two guides have nearly the same guiding performance. On the other hand, the losses in the circular ridge waveguide are much less than those in the conventional ridge waveguide, owing to the absence of sharp edges. The losses accompanied with a sharp edge are due to the axial (parallel to the edge) surface current component which becomes infinite at the edge.

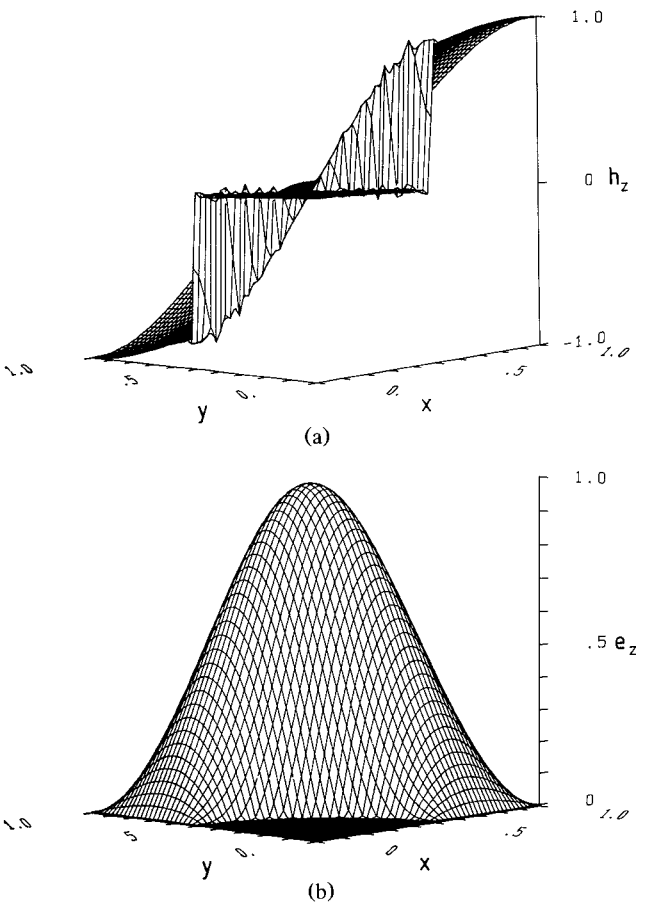

Fig. 8. Three-dimensional plots of (a) the axial magnetic field, h_z, and (b) the axial electric field, e_z, corresponding to the first TE mode and the first TM mode, respectively, in a waveguide with the cross section of Fig. 7(c). Parameters: $(b/a) = 1.0$, $(R/a) = 0.5$.

TABLE III
NORMALIZED CUTOFF WAVENUMBERS $(k_c a/\pi)$ OF THE FIRST FIVE TE MODES

Mode	1	2	3	4	5
Circular ridge	1.0941	1.8348	2.0993	2.5996	2.9067
Conventional	1.0603	1.7001	2.0913	2.5422	2.8856

TABLE IV
NORMALIZED CUTOFF WAVENUMBERS OF THE FIRST FIVE TM MODES

Mode	1	2	3	4	5
Circular ridge	2.3712	3.2088	4.0716	4.2606	4.7436
Conventional	2.4012	3.3139	4.1751	4.3647	4.7434

Finally the electric and magnetic field lines of the first three TE modes and the first three TM modes in a circular ridge waveguide are shown in Fig. 9 and Fig. 10, respectively. The field lines are distributed everywhere over the cross section and are not concentrated near the ridge. In fact, none of these modes is the dominant mode. The dominant mode of the structure does not possess the type of symmetry considered here.

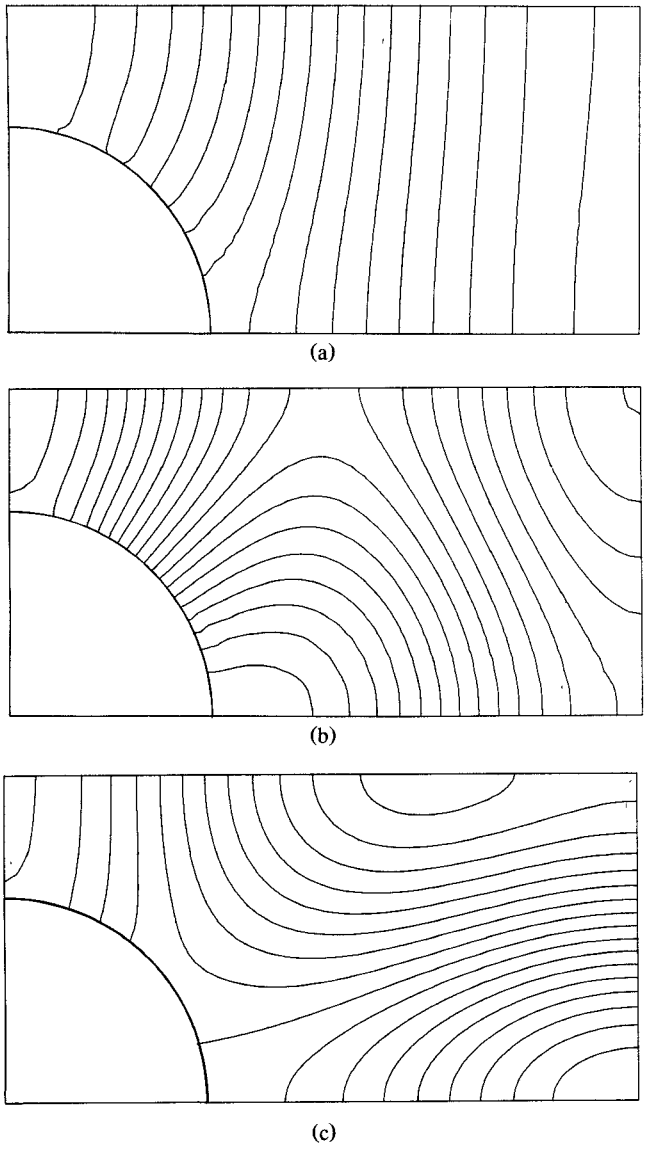

Fig. 9. Electric field lines of the first three TE modes in a circular ridge waveguide: (a) First mode; (b) second mode; (c) third mode. Parameters: $(b/a) = 0.5$, $(R/a) = 0.3$.

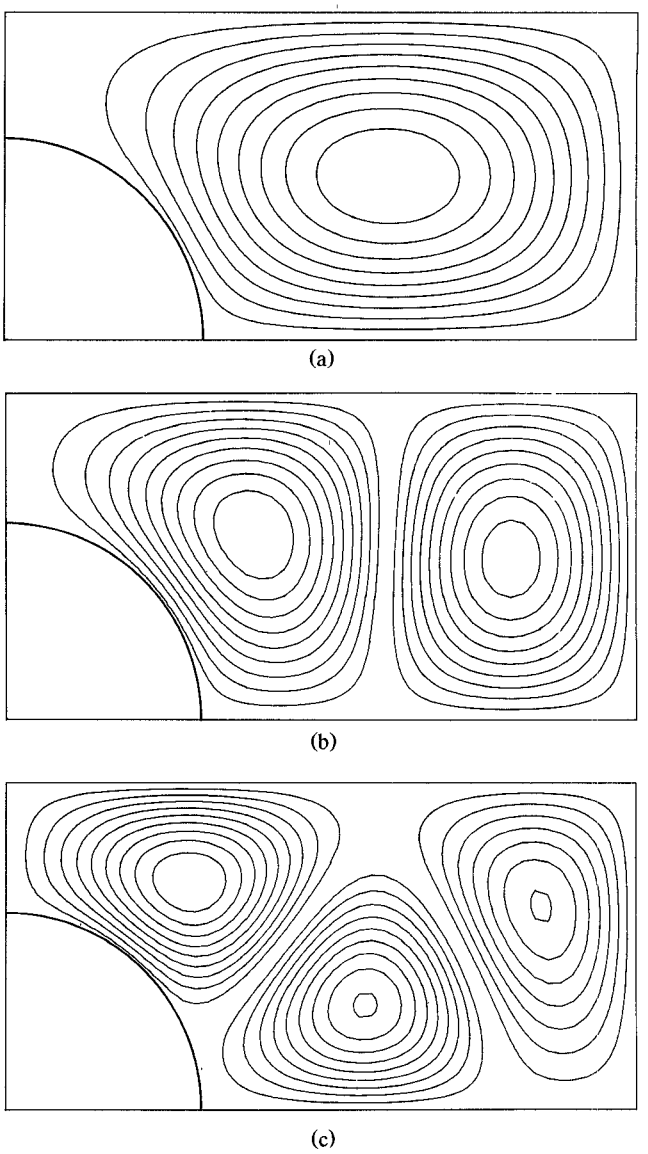

Fig. 10. Magnetic field lines of the first three TM modes in a circular ridge waveguide: (a) first mode; (b) second mode; (c) third mode. Parameters: as in Fig. 9.

V. Conclusion

Rectangular waveguides with rectangular and circular metal inserts have been analyzed by the generalized spectral-domain (GSD) technique, developed in [1]. The analysis has shown that the magnetic field component parallel to a metal edge approaches a constant value (and does not vanish, as the corresponding electric field component does) as the edge is approached. The accuracy of the cutoff wavenumbers has been demonstrated by comparison with the variational analysis. The accuracy of the field distributions has been demonstrated by two- and three-dimensional plots which have shown that the calculated field is negligibly small over the insert's cross section. A CPU time of a few seconds per mode on a Siemens 7.890F is typical. This CPU time is required for the determination of the cutoff wavenumber as well as the field distribution over the guide's cross section. The method then is very sparing of CPU time compared with other methods.

References

[1] A. S. Omar and K. Schünemann, "Analysis of waveguides with metal inserts," *IEEE Trans. Microwave Theory Tech.*, vol. 37, pp. 1924–1932, 1989.

[2] R. Mittra and S. W. Lee, *Analytical Techniques in the Theory of Guided Waves*. New York: Macmillan, 1971.

[3] T. Itoh and R. Mittra, "Spectral-domain approach for calculating the dispersion characteristics of microstrip lines," *IEEE Trans. Microwave Theory Tech.*, vol. MTT-21, pp. 496–499, 1973.

[4] J. B. Davies and D. M.-Syahkal, "Spectral domain solution of arbitrary coplanar transmission line with multilayer substrate," *IEEE Trans. Microwave Theory Tech.*, vol. MTT-25, pp. 143–146, 1977.

[5] T. Itoh and A. S. Hebert, "A generalized spectral domain analysis for coupled suspended microstriplines with tuning septum," *IEEE Trans. Microwave Theory Tech.*, vol. MTT-26, pp. 820–826, 1978.

[6] T. Itoh, "Spectral domain immittance approach for dispersion characteristics of generalized printed transmission lines," *IEEE Trans. Microwave Theory Tech.*, vol. MTT-28, pp. 733–736, 1980.
[7] L.-P. Schmidt and T. Itoh, "Spectral domain analysis of dominant and higher order modes in fin-lines," *IEEE Trans. Microwave Theory Tech.*, vol MTT-28, pp. 981–985, 1980.
[8] P. J. Wood, "TEM line technology for satellite antenna feed applications," in *Proc. Satellite Commun. Conf.* SCC-83, 1983, pp. 29.6.1–4.
[9] M. Abramowitz and I. A. Stegun, *Handbook of Mathematical Functions*. New York: Dover, 1970.
[10] J. Van Bladel, *Electromagnetic Fields*. Washington: Hemisphere, 1985.
[11] Y. Utsumi, "Variational analysis of ridged waveguide modes," *IEEE Trans. Microwave Theory Tech.*, vol. MTT-33, pp. 111–120, 1985.
[12] J. P. Montgomery, "On the complete eigenvalue solution of ridged waveguide," *IEEE Trans. Microwave Theory Tech.*, vol. MTT-19, pp. 547–555, 1971.
[13] R. E. Collin, *Field Theory of Guided Waves*. New York: McGraw-Hill, 1960.

Abbas S. Omar (M'87–SM'89) received the B.Sc. and M.Sc. degrees in electrical engineering from Ain Shams University, Cairo, Egypt, in 1978 and 1982, respectively, and the Doktor-Ing. degree from the Technische Universität Hamburg–Harburg, Germany, in 1986.

From 1978 to 1982, he served as a Research and Teaching Assistant in the Department of Electronics and Computer Engineering of Ain Shams University, where he was engaged in investigations of microstrip lines and below-cutoff waveguides and their use in a hybrid circuit technique for realizing broad-band tunable oscillators. From 1982 to 1983, he was with the Institut für Hochfrequenztechnik, Technische Universität Braunschweig, Germany, as a Research Engineer, where he was involved with theoretical investigations of finlines. From 1983 to 1987 he held the same position at the Technische Universität Hamburg–Harburg, where he was engaged in investigations of planar structures and dielectric resonators. From 1987 to 1990 he was Senior Research Engineer at the Technische Universität Braunschweig. Since 1990 he has been a Professor of Electrical Engineering and head of the field theory group at the Arbeitsbereich Hochfrequenztechnik, Technische Universität Hamburg–Harburg. His current fields of research are concerned with optimization of microwave ovens, field analysis of dielectric resonators, analysis and design of three-dimensional passive systems, theoretical investigations of guiding structures, and the design and optimization of planar structures.

Klaus F. Schünemann (M'76–SM'86) was born in Braunschweig, Germany, in 1939. He received the Dipl.-Ing. degree in electrical engineering and the Doktor-Ing. degree from the Technische Universität Braunschweig in 1965 and 1970, respectively.

Since 1983, he has been a Professor of Electrical Engineering and Director of the Arbeitsbereich Hochfrequenztechnik at the Technische Universität Hamburg–Harburg, Germany. He has worked on nonlinear microwave circuits, diode modeling, solid-state oscillators, PCM communication systems, and integrated circuit technologies such as finline and waveguide below cutoff. His current research interests are concerned with transport phenomena in submicron devices, CAD of planar millimeter-wave circuits, optoelectronics, and high-power millimeter-wave tubes.